Article

Novel Design of Six-Phase Spoke-Type Ferrite Permanent Magnet Motor for Electric Truck Application

Hoyun Won [1], Yang-Ki Hong [1,*], Minyeong Choi [1], Jonathan Platt [1], Briana Bryant [1], Seungdeog Choi [2], Shuhui Li [1], Hwan-Sik Yoon [3], Timothy A. Haskew [1], Jongkook Lee [4], Taegyu Lee [4] and Tae-Won Lim [4]

1   Department of Electrical and Computer Engineering, The University of Alabama, Tuscaloosa, AL 35487, USA; hwon@crimson.ua.edu (H.W.); mchoi11@crimson.ua.edu (M.C.); jtplatt@crimson.ua.edu (J.P.); bmbryant1@crimson.ua.edu (B.B.); sli@eng.ua.edu (S.L.); thaskew@eng.ua.edu (T.A.H.)

2   Department of Electrical Engineering, Mississippi State University, Starkville, MS 35762, USA; seungdeog@ece.msstate.edu

3   Department of Mechanical Engineering, The University of Alabama, Tuscaloosa, AL 35487, USA; hyoon@eng.ua.edu

4   Institute of Fundamental and Advanced Technology (IFAT), Hyundai Motor Company, Uiwang-si 16082, Korea; samemind@hyundai.com (J.L.); xorb9@hyundai.com (T.L.); twlim@hyundai.com (T.-W.L.)

*   Correspondence: ykhong@eng.ua.edu

Abstract: This paper proposes a 300 kW 24-slot/10-pole 6-phase stator-shifted fractional-slot concentrated winding spoke-type ferrite permanent magnet machine for electric truck applications. The proposed motor consists of a stator with dual three-phase windings positioned 75 degrees apart to reduce higher-order MMF harmonic order, and a rotor with an inexpensive and high-resistance ferrite permanent magnet in the spoke configuration. The simulated result of the stator-shifted machine is compared with a fabricated stator-shifted machine, and the results show good agreement with each other. To further reduce the torque ripple from 2.5 to 0.9% while maintaining a high maximum torque of 2980 Nm, circular voids with a diameter of 11 mm are embedded in the rotor. The proposed motor is evaluated for irreversible demagnetization, mechanical and thermal stability, and fault tolerant ability. To assess the proposed motor performance, the electric truck simulation model is constructed using MATLAB/Simulink and used to compare with the reported 12-slot/10-pole rare-earth permanent magnet-based machine. Compared to a previously reported six-phase rare-earth permanent magnet based flat-type machine, the proposed motor can save 4.3 kWh of energy with a USD 2512 lower cost while retaining a similar motor performance.

Keywords: phase-shift; rare-earth free permanent magnet; six-phase winding; spoke-type motor

1. Introduction

Throughout the world, many municipal governments have announced the replacement of diesel transit buses with electric buses to reduce the air pollution in cities [1–3]. Eliminating diesel exhaust emissions from the diesel transit buses by replacing them with electric buses not only improves the air quality by eliminating 2 million tons of greenhouse gas emissions each year, but also delivers financial benefits, including reduced maintenance and fuel cost by USD 200,000 over the lifetime of the bus, and societal benefits, including reduced health care expenses caused by air pollutants [1–3]. It is reported that air pollutants can cause heart attacks, premature deaths, asthma, and other severe health issues. The transit bus is classified as class-7 heavy-duty truck (HDT), which also covers most of the city vehicles, such as street sweepers, garbage, beverage, and furniture trucks. Accordingly, electrifying the class-7 HDTs is essential to substantially reduce air pollution in the city.

Among the reported electric motors used for HDTs, multi-phase rare-earth permanent magnet (RE-PM)-based synchronous machines are widely utilized due to their high

torque and power density, maximum speed, and efficiency [1]. For multi-phase machines, fractional-slot concentrated winding (FSCW) is generally utilized because the FSCW provides the inherent fault-tolerant capability, higher winding factor, and lower cogging torque than distributed winding [4–6]. However, the FSCW produces unwanted space harmonics in the stator magnetomotive force (MMF), resulting in high eddy current losses in permanent magnet (PM), localized core saturation, and difficulty to produce high reluctance torque from interior-mounted rotor topology [7,8].

To suppress the stator MMF harmonics, various methods, including PM segmentation [4,5], multilayer winding design [9], coils with a different number of turns per coil side [10], and stator-shifting [11], have been reported. Among these MMF harmonic suppression methods, the stator-shifting concept reduces both sub- and high-order stator MMF harmonics effectively without increasing manufacturing costs and material usage [4–6,11]. This concept has been validated with various rotor topologies, including surface-mounted and interior-mounted single- and multi-layer V-type rotor topologies [4–6]. However, this concept has not been validated for interior-mounted spoke-type rotor topology yet.

For HDTs, rare-earth NdFeB magnets are widely used for permanent magnet synchronous machines (PMSMs) to achieve high torque density, efficiency, and maximum speed by exploiting its high maximum energy product $(BH)_{max}$. However, NdFeB RE-PM suffers from high and volatile cost, unstable supply, complicated manufacturing processes, and low electrical resistivity [12,13]. The traction motors of HDTs need PMs with a lower price and more stable supply than the motors used in light-duty vehicles because a high peak power rating in the range from 300 to 360 kW is required for HDTs [1]. The motor must be large enough to produce such a high peak power, requiring a large PM volume. Further, the high electrical resistivity of PM is essential for the motor employing the FSCW winding to minimize the temperature of the PM. The PM temperature rises by the eddy current loss caused by higher-order space harmonics. Thereby, a cost-effective and high electrical resistive PM is demanded to address the above issues.

Among such PMs, hard ferrite shows the most viable solution. Ferrite has USD 86–93 lower cost and 6667-times higher electrical resistivity than NdFeB PM [14]. However, the ferrite-based PM motors suffer from low torque density due to the relatively low magnetization. One of the ways to address this drawback is to employ spoke-type interior-mounted rotor topology. This topology arranges the ferrite PMs in oriented planes to increase the air-gap flux by focusing the PM flux and increasing the reluctance torque [15]. However, this design results in significant flux density distortion in the air gap, causing a high torque ripple. Although many methods, from design-based to control-based, have been reported to minimize the torque ripple, they either decrease the maximum torque or increase an unbalanced axial electromagnetic force [16].

In the previous paper [17], we reported a novel 24-slot/10-pole 6-phase stator-shifted FSCW spoke-type ferrite interior PMSM (6Φ-SS-FSCW-Fer-SIPMSM), exhibiting a peak power of 250 kW, peak torque of 2150 Nm, and torque ripple of 4.1%. The circular-notch torque ripple reduction method and the stator-shift concept were introduced and explained.

In this paper, the proposed 6Φ-SS-FSCW-Fer-SIPMSM is scaled up to produce a peak power of 300 kW, peak torque of 2980 Nm, and torque ripple of 0.9% for quantitative comparison with the reported 300 kW 12-slot/10-pole 6-phase FSCW NdFeB-based flat-type IPMSM (6Φ-FSCW-Nd-FIPMSM) [3]. The circular-notch torque ripple reduction method and stator-shift concepts are further advanced and quantitatively analyzed via winding-function theory, harmonic spectrum analysis, and flux distributions in the motor. In addition, the proposed 6Φ-SS-FSCW-Fer-SIPMSM performance is compared with the conventional 12-slot/10-pole 6-phase FSCW spoke-type ferrite interior PMSM. Lastly, the electric truck model, constructed with MATLAB/Simulink, is used to evaluate the proposed motor performance and efficiency, and for comparison with the reported 6Φ-FSCW-Nd-FIPMSM.

2. Initial Motor Design and Validation

Recently, Morozov et al. evaluated the performance of five 12-slot/10-pole 6Φ-FSCW-Nd-FIPMSM, having various power ratings of 150, 200, 250, 300, and 350 kW, with 4 gearboxes from 3- to 6-speed [3]. Class-7 HDT simulation was performed under various drive cycles. The simulation result show that a 300 kW 12-slot/10-pole 6Φ-FSCW-Nd-FIPMSM with a 3-speed gearbox satisfies the required performance goals of 27 s acceleration time from 0 to 60 mph, 30% starting grade, and 113 km/h top speed with good energy efficiency [3]. Thus, the reported 300 kW 12-slot/10-pole 6Φ-FSCW-Nd-FIPMSM was chosen as a benchmark motor in this paper and investigated more thoroughly.

Table 1 shows the specification of the benchmark motor [3], while Figure 1a shows the schematic of the reported benchmark motor. With the given specification in Table 1, the reported 6Φ-FSCW-Nd-FIPMSM was designed and simulated using ANSYS Maxwell 2D finite-element-analysis (FEA) v.18.1 to validate the reported motor performance. Because the reported literature did not provide a specific grade of Nd-Fe-B PM, the reported 6Φ-FSCW-Nd-FIPMSM with various grades of the Nd-Fe-B PM was first simulated to determine the grade of Nd-Fe-B PM used in the literature. The simulation results show that N42UH grade Nd-Fe-B PM, which has remanent flux density of 1.28 T and coercivity of 955 kA/m at room temperature [18], produces same maximum torque of 3110 Nm as reported by the authors of [3].

Table 1. Specifications of benchmark motor. Data from [3].

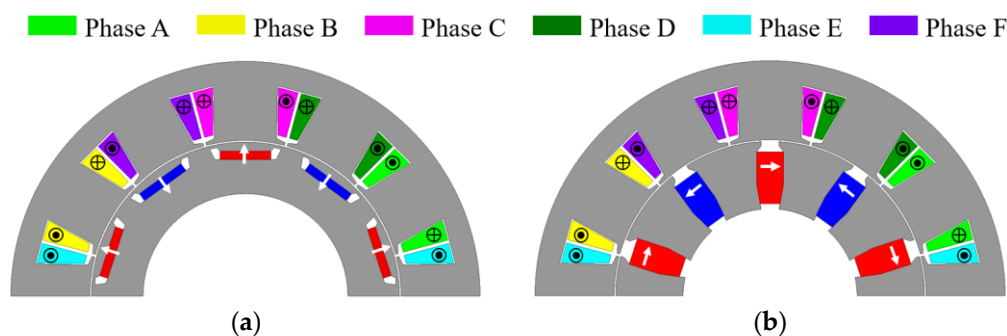| Parameter	Value
Stator outer/inner diameter [mm]	550/366
Rotor outer/inner diameter [mm]	362/196
Stack length [mm]	300
Number of slots/poles	12/10
Number of turns	64
Number of parallel paths	8
Rated/peak current density [A/m^2]	6.3/16.4
Rated/peak current [A$_{rms}$]	250/636
Copper mass [kg]	135
Maximum torque [Nm]	3110
Soft iron core material	M19–29G

Figure 1. Schematic of 6-phase 12-slot/10-pole (**a**) reported flat-type IPMSM and (**b**) proposed spoke-type IPMSM.

To observe the effect of the ferrite PM on motor performance, the reported 6Φ-FSCW-Nd-FIPMSM was simulated with Hitachi's NMF-12G ferrite PM, which has a remanent flux density of 0.45 T and coercivity of 334 kA/m at room temperature. Due to lower magnetic properties of the ferrite PM than Nd-Fe-B PM, the torque at peak current was significantly reduced from 3110 to 1550 Nm (50% reduction), as shown in Figure 2. In order to improve the torque, four different rotor topologies, including PM-assisted synchronous reluctance machine (PMASynRM), V-type PMSM, surface-mounted PMSM (SPM), and

spoke-type PMSM, were simulated and investigated under the same motor specifications, operating conditions, and NMF-12G ferrite PM as in our previous studies [17]. The simulation results show that among the above topologies, the spoke-type topology, which is shown in Figure 1b, delivered the highest torque of 2320 Nm and relatively low back EMF at 3000 rpm, but suffered from high torque ripple. Compared to the reported flat-type topology, the spoke-type topology increased the maximum torque from 1550 to 2320 Nm (49.7% improvement), as shown in Figure 2. This is mainly attributed to the flux concentration effect of the spoke type topology [19] and increased PM volume. The motor, having this spoke-type rotor topology, and the FSCW winding were simulated and verified experimentally by the authors of [19], who showed that the rotor sustained its operation up to 14,000 rpm without mechanical breakdown.
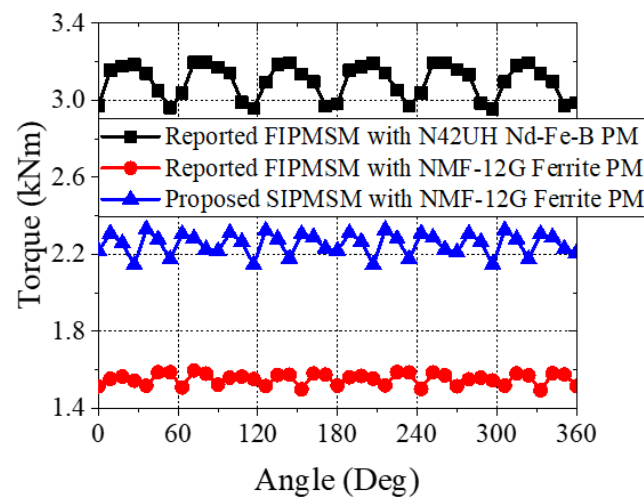

Figure 2. Maximum torque performance of the reported FIPMSM with N42UH Nd-Fe-B PM and NMF-12G ferrite PM and proposed SIPMSM with NMF-12G ferrite PM.

2.1. Winding Configuration

A typical dual 3Φ 12-slot/10-pole configuration with a double layer winding is shown in Figure 3a. According to the authors of [4], the most detrimental MMF harmonics are those close to the torque-producing harmonic. For the five pole-pair motor, the detrimental MMF harmonics are the first and seventh harmonic, whereas the torque-producing harmonic is the fifth harmonic. It was reported that when the phases of the two three-phase windings are shifted by 30°, all harmonics below the torque-producing harmonic can be canceled [20]. However, the harmonics above the torque-producing harmonic, which is the seventh harmonic, remain.

Thus, the concept of stator-shifting was employed to minimize the seventh harmonic by shifting one of the dual three-phase windings with a specific mechanical angle (α) against another three-phase winding, as illustrated in Figure 4. The number of slots and coil pitches must be doubled from 12 to 24 and from 1 to 2, respectively, to accommodate the shifted 3-phase winding. The number of turns was halved from 64 to 32 to maintain the same total copper volume. An optimal α that minimizes the seventh harmonic can be calculated using a winding function theory [16]. Based on the winding function theory, the MMF of the unshifted and α-shifted three-phase winding are:

$$F_1(\theta, t) = \sum_{k=1,-5,7}^{\infty} \frac{12 N_c I_m}{k\pi} \sin\left(\frac{k\pi}{12}\right) \cdot \sin\left(\frac{(k-1)\pi}{12}\right) \cdot \sin\left(k\theta - \omega t - \frac{(k-1)\pi}{12}\right) \tag{1}$$

$$F_2(\theta, t) = \sum_{k=1,-5,7}^{\infty} \frac{12 N_c I_m}{k\pi} \sin\left(\frac{k\pi}{12}\right) \cdot \sin\left(\frac{(k-1)\pi}{12}\right) \cdot \sin\left(k\theta - \omega t - k\alpha - \frac{(k-1)\pi}{12}\right) \tag{2}$$

where N_c is the number of turns, I_m is the peak phase current, and k is the harmonic order. The negative k for the fifth harmonic is required to account for the harmonic sequence

direction. Since N_c and I_m were the same for both windings, the total MMF (F_t) was calculated by adding F_1 and F_2, resulting in Equation (3).

$$F_t(\theta, t) = F_1(\theta, t) + F_2(\theta, t) = \sum_{k=1,-5,7}^{\infty} \frac{24 N_c I_m}{k\pi} \sin\left(\frac{k\pi}{12}\right) \cdot \sin\left(\frac{(k-1)\pi}{12}\right) \cdot \cos\left(\frac{k\alpha}{2}\right) \cdot \sin\left(k\theta - \omega t - \frac{k\alpha}{2} - \frac{(k-1)\pi}{12}\right) \qquad (3)$$

where the sum to product trigonometric identifies for sine is used to simplify the equation. As Equation (3) suggests, one of the simple and effective ways to cancel the seventh harmonic is to find the α that can make the term $\cos(k(\alpha/2))$ equal to zero for $k = 7$. The optimal α is 77.14°. However, realizing such α requires an uneven tooth width. Instead, the α closest to the optimal α and in multiples of tooth pitch, i.e., multiplication of 360°/24 = 15°, meet the requirement. The closest value to the optimal angle of 77.14° and yielding an integer multiple to tooth pitch is 75°, which corresponds to five slots apart from each winding. Figure 3b illustrates the proposed 24-slot/10-pole 6Φ-SS-FSCW-Fer-SIPMSM with an α of 75°.
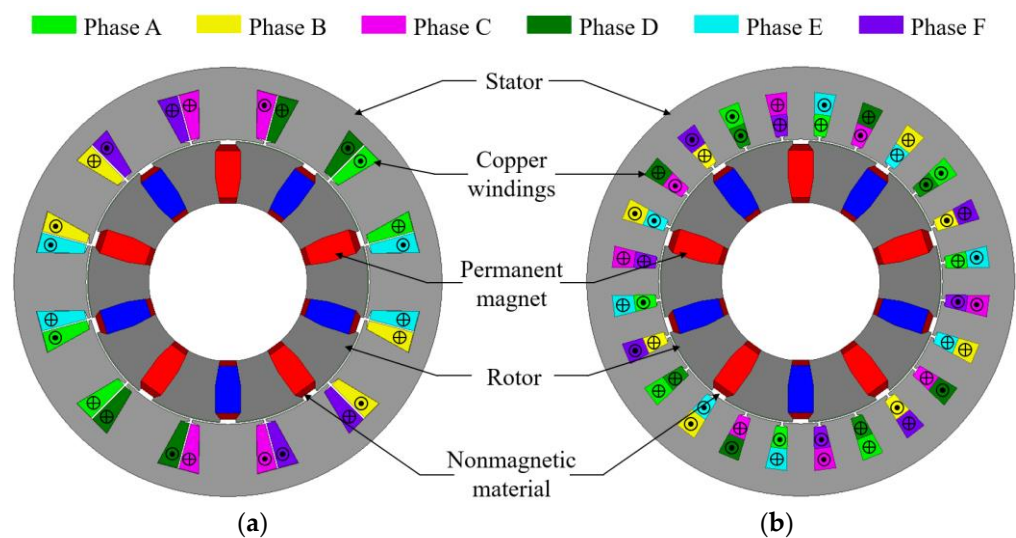

Figure 3. Schematic of 6-phase (**a**) 12-slot/10-pole unshifted and (**b**) 24-slot/10-pole stator-shifted FSCW winding layout.
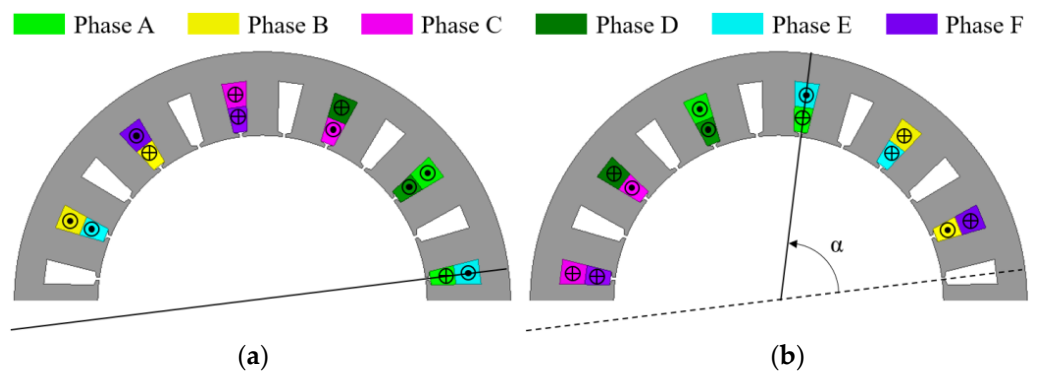

Figure 4. Design of (**a**) first and (**b**) second set of the 12-slot/10-pole winding layout.

The MMF distribution and corresponding harmonic spectrum of the conventional 12-slot/10-pole unshifted and the proposed 24-slot/10-pole shifted 6-phase PM machine are shown in Figure 5. As Figure 5b indicates, the stator-shifting design significantly decreased not only the 7th harmonic from 0.79 to 0.1 (87.3% reduction), but also other higher-order harmonics, such as the 17th harmonic, from 0.375 to 0.03 (92% reduction), the 19th harmonic from 0.36 to 0.26 (27.8% reduction), and the 29th harmonic from 0.2 to 0.16

(20% reduction). Hence, the corresponding winding layout with a 75° shift was selected and employed throughout this paper.
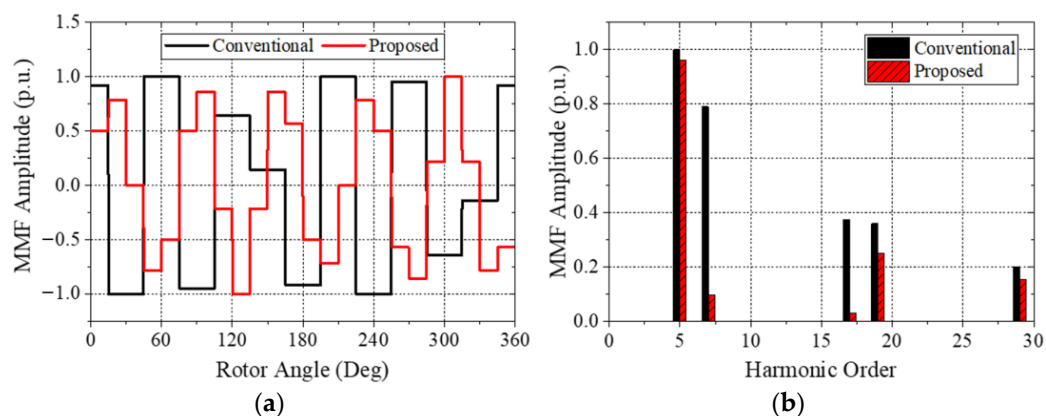

(a)   (b)

Figure 5. Total MMF distribution (**a**) profile and (**b**) harmonic spectrum of the conventional and proposed FSCW motor.

To validate the simulation results of the proposed 24-slot/10-pole 6Φ-SS-FSCW-Fer-SIPMSM, the reported 6-phase 18-slot/8-pole V-type IPMSM with a 20° electrical phase shift between two three-phase windings [4] was designed and simulated using ANSYS Maxwell 2D FEA v.18.1. Figure 6 shows the designed motor with a winding layout and prototype. The simulated back electromotive force (EMF) waveforms of the A-B-C windings at 2800 rpm using an in-house FEA tool were investigated and compared with the back EMF waveforms of the A-B-C windings that were measured and reported by the authors of [4]. Figure 7 shows the corresponding performance comparison. As shown, the simulated back EMF shows good agreement with the measured back EMF.

(a)   (b)   (c)
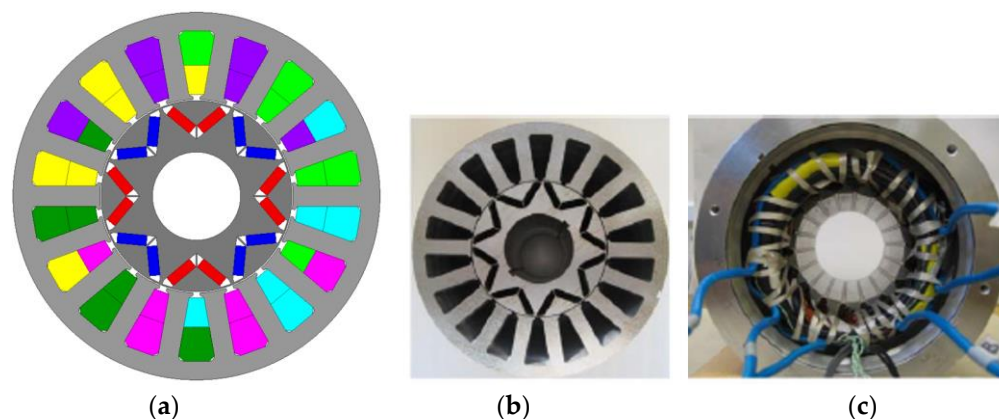
Figure 6. The 6-phase 18-slot/8-pole machine: (**a**) schematic with winding layout and top view of the motor, (**b**) without copper coil and PM, and (**c**) with copper coil and others [4]. ©IEEE. Reprinted with permission from Patel, V.; Wang, J.; Wang. W.; Chen, X. The 6-phase fractional-slot-per-pole-phase permanent-magnet machines with low space harmonics electric vehicle application. IEEE Transactions on Industry Application, vol. 50, no. 4, July 2014.
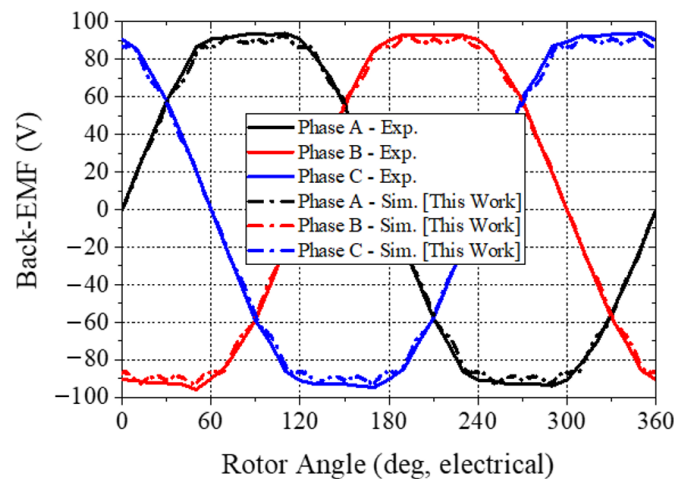
Figure 7. Comparison of measured [4] and simulated back EMFs of Phase A, B, and C windings at the base speed of 2800 rpm.

2.2. Electromechanical Performance Comparison

The maximum torque, torque ripple (T_{rip}), cogging torque (T_{cog}), and back-EMF harmonic spectrum of the conventional 12-slot/10-pole unshifted and the proposed 24-slot/10-pole shifted 6-phase spoke-type ferrite IPMSM were simulated and compared. The specifications of the conventional and proposed motors are summarized in Table 2. The simulated maximum torque, T_{rip}, T_{cog}, and total harmonic distortion (THD) of the back-EMF of the conventional and proposed motors are presented in Table 3. The T_{rip} was calculated by Equation (4).

$$T_{rip} = \frac{T_{max} - T_{min}}{(T_{max} + T_{min})/2} \tag{4}$$

where T_{max} and T_{min} are the maximum and minimum torque magnitude, respectively. It is noted that the proposed stator-shifted machine increased the maximum torque from 2320 to 2970 Nm (28% improvement), and decreased the T_{rip} from 10.9 to 2.5% (77.1% reduction) without affecting the T_{cog} compared to the conventional unshifted machine. The significant increase in the maximum torque is mainly attributed to the increased air gap flux density. Figure 8 shows the air gap flux density at maximum current. Further, the T_{rip} reduction of 77.1% may be attributed to the suppression of the 8th, 9th, 11th, 13th, 15th, and 17th harmonics in back-EMF, as shown in Figure 9. The suppression led to 11.3% less THD compared to the conventional unshifted motors.

Table 2. Specifications of the conventional and proposed motor.

Parameter	Conventional	Proposed
Stator outer/inner diameter [mm]	550/366	
Rotor outer/inner diameter [mm]	362/196	
Stack length [mm]	300	
Number of slots/poles	12/10	24/10
Number of turns	64	32
Number of parallel paths	8	8
Coil pitch	1	2
Rated/peak current density [A/m^2]	6.3/16.4	
Rated/peak current [A$_{rms}$]	250/636	

Table 3. Performance comparison between the conventional and proposed motor.

Parameter	Conventional	Proposed
Maximum torque [Nm]	2320	2970
Torque ripple (T_{rip}) [%]	10.9	2.5
Cogging torque (T_{cog}) [Nm]	3.3	3.3
Total harmonic distortion (THD) of back-EMF at 2000 rpm [%]	37.3	33.1
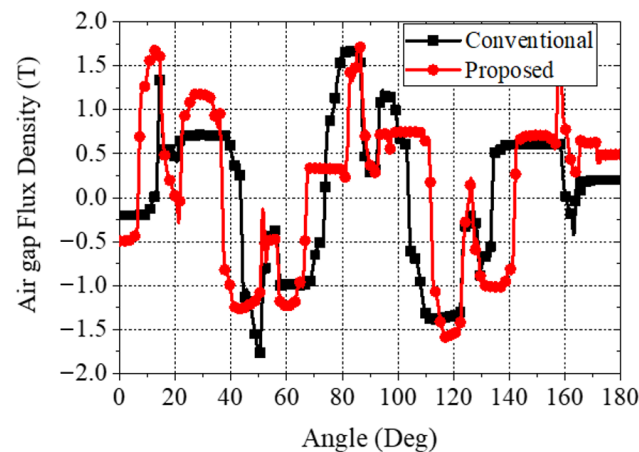
Figure 8. Air gap flux density at the maximum current.
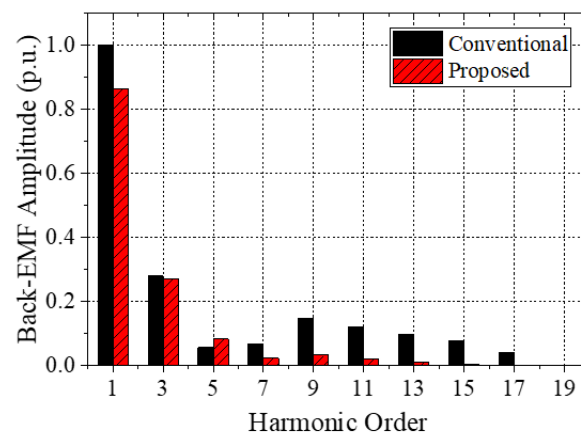
Figure 9. Comparison of normalized back-EMF space harmonic distribution profile of the conventional and proposed motor.

3. Optimal Motor Design and Specification

In this section, the T_{rip} reducing circular notch method is discussed. The efficiency map with torque versus speed characteristics of the proposed 6Φ-SS-FSCW-Fer-SIPMSM was constructed and compared with the reported 6Φ-FSCW-Nd-FIPMSM. After the mechanical stress analysis at the maximum speed and the thermal analysis at the peak power, the irreversible demagnetization analysis was conducted to assess the reliability of the proposed motor at extremely low temperature of $-40\,°C$ and regular temperature at $80\,°C$.

3.1. Torque Ripple Reducing Circular Notch

Despite the small 2.5% T_{rip} of the proposed motor, the T_{rip} needs to be further decreased to reduce any stress affecting mechanical parts of the motor. One circular notch, having a diameter of 10 mm, was introduced on the edge of the rotor near the air gap to achieve T_{rip} reduction, as shown in Figure 10. A nonmagnetic shaft with a rectangular notch was

also introduced to hold the rotor in one piece and rotate it. The performances of 6Φ-SS-FSCW-Fer-SIPMSM with and without the circular notch and a rectangular cavity-based nonmagnetic shaft are summarized in Table 4. A circular notch, having a diameter of 10 mm on the rotor, significantly decreased the T_{rip} from 2.5 to 1.2% (53% reduction) while retaining the maximum torque. This is mainly attributed to the 0.3–0.4 T increased flux density in the blue dashed rectangular region in Figure 11b compared to the flux density in the blue dashed rectangular area in Figure 11a. This high flux density results in a 10.8% reduction in THD of back-EMF, which may be the main reason for the 53% reduction in the T_{rip}.
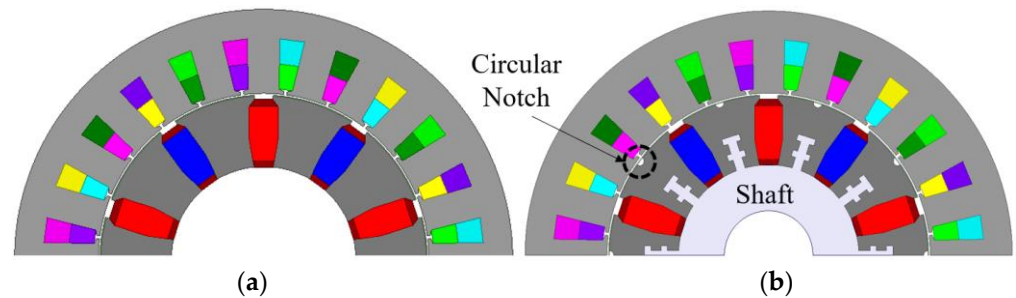

(a) (b)

Figure 10. Design of 6Φ-SS-FSCW-Fer-SIPMSM (**a**) without and (**b**) with circular notch on the rotor and rectangular nonmagnetic shaft fixture.

Table 4. Performance comparison between conventional and proposed motor.

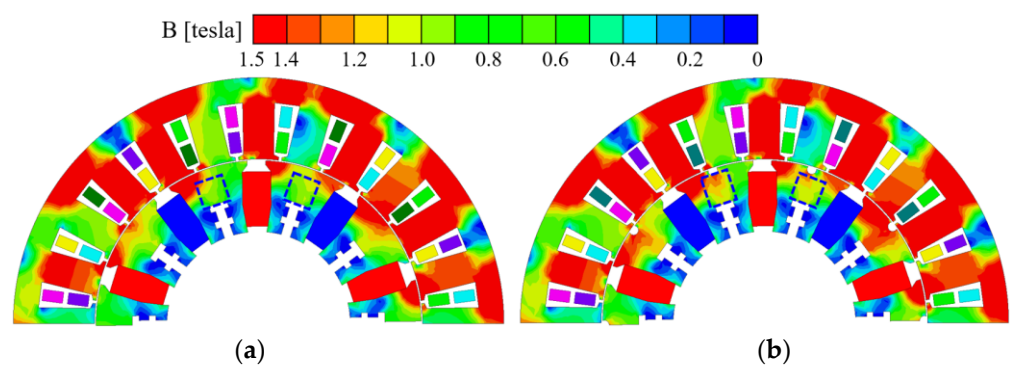| Parameter	No Notch	Circular Notch on Rotor	Notch with Shaft
Torque [Nm]	2970	2980	2980
Torque ripple [%]	2.5	1.2	1.2
Torque ripple difference from no circular void [%]	-	53	53

(a) (b)

Figure 11. Flux density distribution of 6Φ-SS-FSCW-Fer-SIPMSM with (**a**) shaft only and (**b**) shaft and circular notch on the rotor.

A parametric study ws conducted to investigate the effects of circular notch diameter on the maximum torque and T_{rip}. Figure 12 shows the maximum torque, T_{rip}, and the T_{cog} of the proposed 6Φ-SS-FSCW-Fer-SIPMSM as a function of the circular notch diameter. The maximum torque was unaffected by the circular notch diameter, as shown in Figure 12a, while the T_{rip} showed a positive quadratic trend. The lowest T_{rip} of 0.9% (64% reduction compared to that of the motor without notch) was observed for the motor having a circular notch with a diameter of 11 mm, which was also equivalent to 3.04% of outer rotor diameter. This reduction was mainly due to the lowest cogging torque at 11 mm diameter, as shown in Figure 12b. In summary, although the introduction of the circular notch may increase the manufacturing process and cost, the significant T_{rip} of the motor can be reduced to 0.9%,

which can decrease the cost of shock absorbing materials and components. Figure 13 shows the detailed schematic of the proposed 6Φ-SS-FSCW-Fer-SIPMSM, while Table 5 shows the detailed machine dimensions.
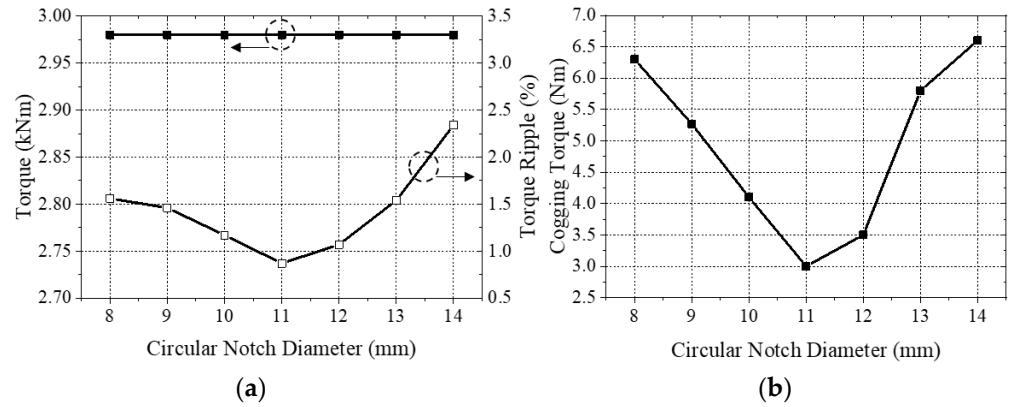
Figure 12. (**a**) Maximum torque and torque ripple performance and (**b**) cogging torque with respect to the diameter of the circular notch used on the rotor.

Figure 13. Geometrical parameters of the proposed 6Φ-SS-FSCW-Fer-SIPMSM.

Table 5. Machine dimensions of the proposed 6Φ-SS-FSCW-Fer-SIPMSM.

Parameter	Symbol	Value [mm]
Stator		
Yoke height	H_y	32
Upper slot width	W_{su}	27.5
Bottom slot width	W_{sb}	15
Slot height	H_s	55
Tooth width	W_t	36
Slot opening height	H_{so}	3.3

Table 5. *Cont.*

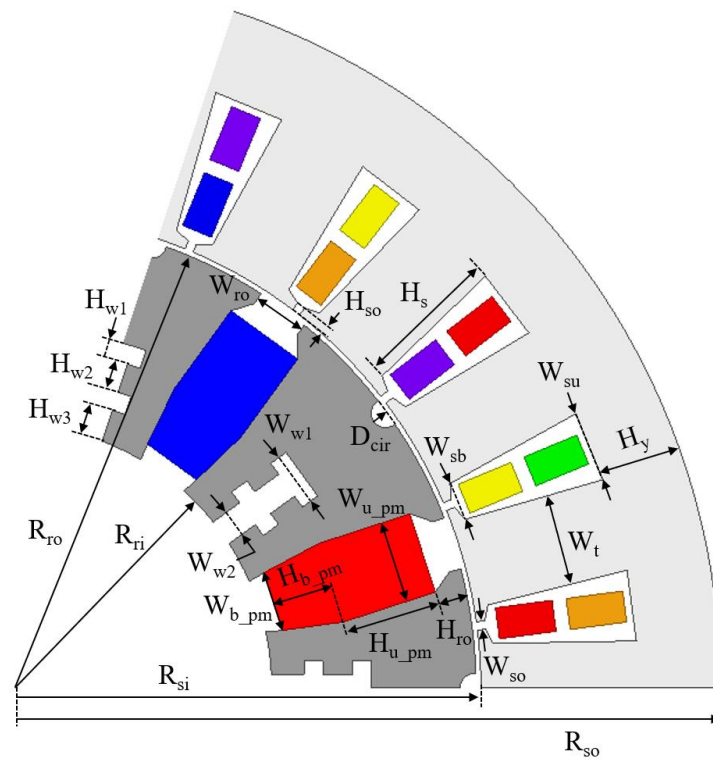| Parameter	Symbol	Value [mm]
Stator		
Slot opening width	W_{so}	3.3
Outer stator radius	R_{so}	275
Inner stator radius	R_{si}	183
Rotor		
Rotor opening height	H_{ro}	12.1
Rotor opening width	W_{ro}	20.5
Rectangular cavity 1 height	H_{w1}	7.3
Rectangular cavity 2 height	H_{w2}	11.4
Rectangular cavity 3 height	H_{w3}	12.6
Rectangular cavity 1 width	W_{w1}	20.8
Rectangular cavity 2 width	W_{w2}	10.4
Circular notch rotor	R_{cir}	5.5
Outer rotor radius	R_{ro}	181
Inner rotor radius	R_{ri}	98
Permanent Magnet		
Upper permanent magnet width	W_{u_pm}	31.7
Bottom permanent magnet width	W_{b_pm}	23.3
Upper permanent magnet height	H_{u_pm}	37.1
Bottom permanent magnet height	H_{b_pm}	23.8

3.2. Efficiency Map

The efficiency map with the torque-speed characteristics was drawn to evaluate the proposed motor's base (ω_{base}) and maximum speed (ω_{max}) and power efficiency (η). The η at the desired motor torque (T_m) and speed (ω_m) is calculated by Equation (5).

$$\eta = \frac{P_{out}}{P_{in}} = \frac{T_m \omega_m}{T_m \omega_m + P_{cu} + P_{iron}} \tag{5}$$

where P_{in} and P_{out} are the input and output power, respectively, and P_{cu} and P_{iron} are the copper and iron loss, respectively. These losses are given by Equations (6) and (7),

$$P_{cu} = 6 I_{rms}^2 R_s \tag{6}$$

$$P_{iron} = K_h f B_m^2 + K_e f^2 B_m^2 \tag{7}$$

where R_s is the stator winding resistance; f is the frequency in Hz; K_e and K_h are the coefficient of eddy-current and hysteresis loss, respectively; and B_m is the magnetic flux density. For K_e and K_h, 0.409 and 164.2 were used, respectively.

The maximum torque per ampere (MTPA) control was utilized to find the optimal current and current angle to produce the maximum torque until ω_m reaches ω_{base}. ω_{base} is a speed when the back-EMF of the motor reaches the maximum dc-link voltage (V_{dc_link}), which can be calculated by Equation (8),

$$V_{dc\_link} = V_{bat} / \sqrt{3}, \tag{8}$$

where V_{bat} is the battery dc voltage. Dividing V_{bat} by a square root of 3 is needed because the space-vector pulse width modulation (SV-PWM) limits V_{bat} at the expense of modulating voltage-fed inverter [21]. Above the base speed, the flux weakening control was applied to extend the motor operation until ω_m reached ω_{max}. The motor reached its ω_{max} when both back-EMF and operating current reached a V_{dc_link} of 433 V and current limit of 636 A_{rms}.

By utilizing the above equations and control, the power efficiency map of the proposed 24-slot/10-pole 6Φ-SS-FSCW-Fer-SIPMSM was drawn, as shown in Figure 14a. The motor retained the constant maximum torque of 2980 Nm until the motor speed reached 1500 rpm, i.e., ω_{base}, and sustained its operation until the speed reached 3750 rpm, i.e., ω_{max}. The peak

η was higher than 97% when the ω_m was between 250 to 2750 rpm, and the T_m was below 600 Nm.
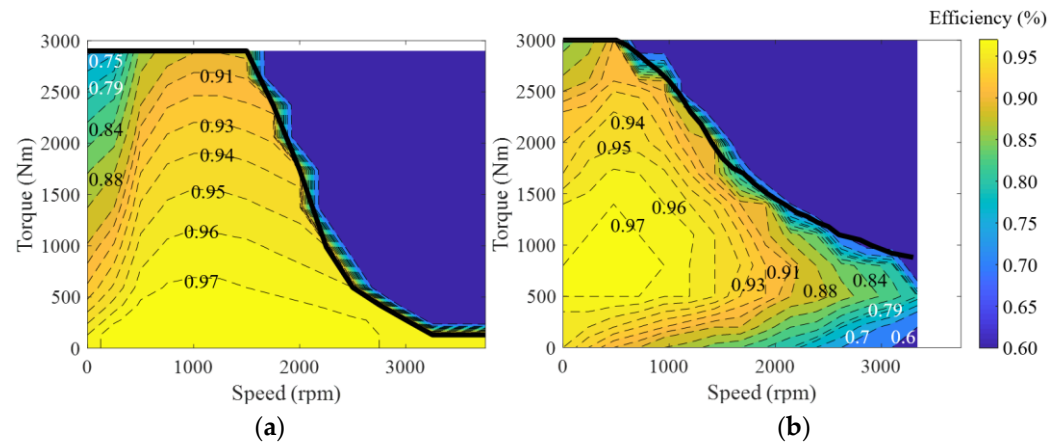

Figure 14. Efficiency map with torque-speed characteristic of (**a**) proposed 6Φ-SS-FSCW-Fer-SIPMSM and (**b**) conventional 6Φ-FSCW-Nd-FIPMSM.

For comparison, the efficiency map of the benchmark 300 kW 12-slot/10-pole RE-PM 6Φ-FSCW-Nd-FIPMSM was imported from [3] and plotted in Figure 14b. The motor exhibited a maximum torque of 3100 Nm, ω_{base} of 500 rpm, and ω_{max} of 3250 rpm, with a peak η above 97% region for ω_m between 0 and 1000 rpm and T_m between 500 and 1250 Nm. Compared to the benchmark RE-PM motor, the proposed ferrite motor exhibited 1000 rpm and 500 rpm higher ω_{base} and ω_{max}, respectively, and 80% larger η of 97% region with only 3.9% lower maximum torque.

3.3. Mechanical Analysis

Mechanical FEA analysis was conducted to validate the mechanical stability of the motor at the ω_{max} of 3750 rpm using ANSYS Mechanical. Figure 15 shows the Von Mises stress distribution in the rotor lamination, rotor shaft, and the bottom wedge of the proposed 6Φ-S-FSCW-Fer-SPMSM at 3750 rpm. As shown in Figure 15, the maximum stress occurred at the contact surface between the rotor lamination and the nonmagnetic shaft. The calculated Von Mises stresses in all these parts are well below the stress limit, which is 345 MPa for the M19 rotor lamination, 586 MPa for the CuBe alloy rotor shaft, and 138 MPa for the non-metallic composite rotor wedge.
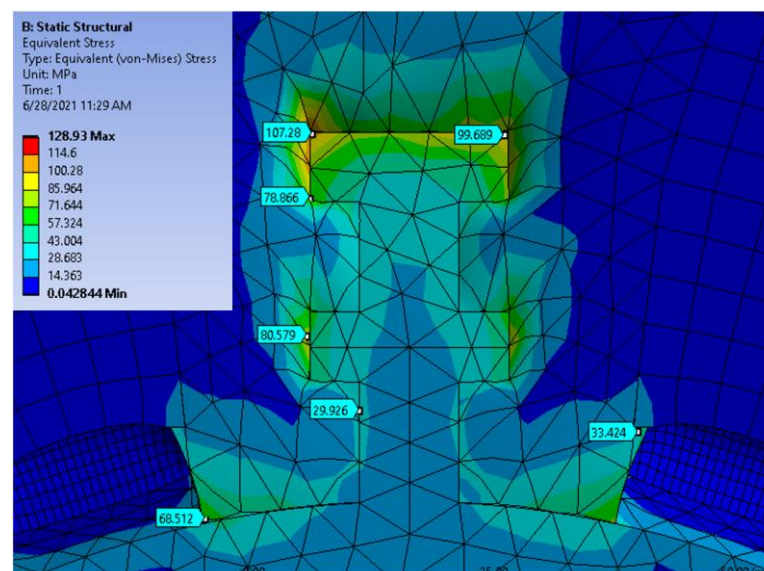

Figure 15. Mechanical analysis of the proposed 6Φ-S-FSCW-Fer-SPMSM at 3750 rpm.

3.4. Thermal Analysis

Thermal FEA analysis was conducted to validate the thermal stability of the motor at maximum power, where the current was at its peak of 690 A_{rms} and speed was at its base speed of 1750 rpm. Table 6 summarizes the thermal conductivity of each component [19,22,23], while Table 7 shows the power loss density of each component. Due to the high resistance of the ferrite PM, the eddy-current loss of the PMs was negligible. Thus, the PM eddy-current loss was not included in the simulation. To cool the motor, the cooling system used in [19] was utilized. The details regarding the cooling system have been described by the authors of [19]. Figure 16 shows the FEA results at the maximum power. As clearly shown, the maximum temperature of the rotor was about 74–76 °C, which is well within the thermal limits of the permanent magnet. In comparison, the maximum temperature of the stator was around 180 °C, which occurred near the copper winding and is within the thermal limits of the class H insulation.

Table 6. Thermal conductivity of the components used in the simulation. Data from [19,22,23].

Component	Thermal Conductivity [W/(mK)]	Material
Stator/Rotor	48	Silicon steel
Shaft	105	CuBe alloy
Winding	387.6	Copper
Air gap	0.429	Air
Permanent magnet	1	Ferrite
Rotor wedges	0.1	Non-metallic composite

Table 7. Power loss density of the components at maximum power.

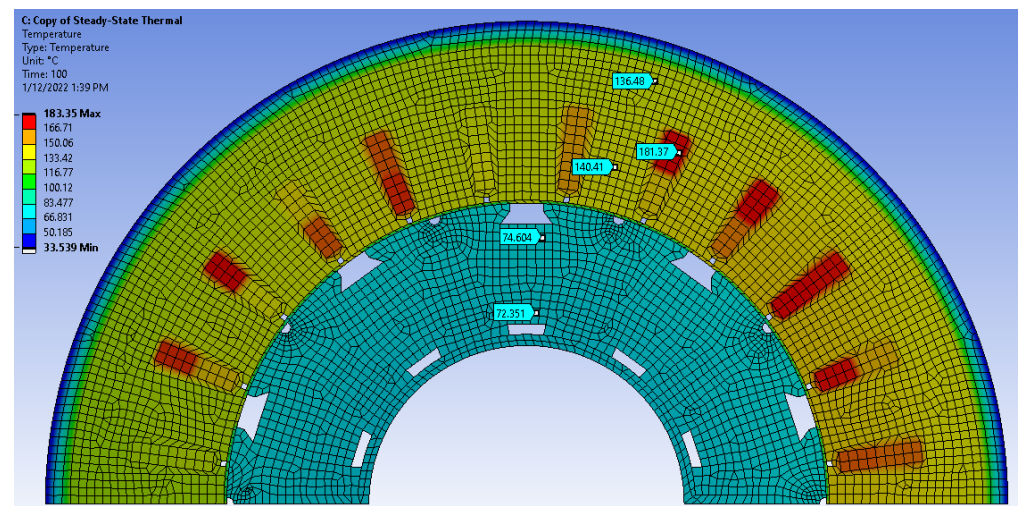| Component	Power Loss Density [W/m^3]
Stator	1,111,863
Rotor	83,169.6
Winding	1,744,287.42

Figure 16. Thermal analysis of the proposed 6Φ-S-FSCW-Fer-SPMSM at maximum power.

3.5. Demagnetization Analysis

Due to the inherent low coercivity of the ferrite PM and positive temperature coefficient of the intrinsic coercivity, analyzing the irreversible demagnetization rate at the low (−40 °C) and high temperature (80 °C) is essential. Table 8 shows the magnetic properties of NMF-12G at −40 and 80 °C [24]. Further, it should be noted that the PM, whose flux density (B) or magnetic field (H) was below the knee point B value (B_{thr}) or exceeded knee

point H value (H_{thr}), was irreversibly demagnetized [14]. The B_{thr} and H_{thr} were 0.08 T and 330 kA/m at −40, and −0.1 T and 380 kA/m at 80 °C, respectively. Figures 17 and 18 show the *B* and *H* distribution of the ferrite PM under 2.6× and 2.8× rated current at −40 °C, and under 2.6× and 3.4× rated current at 80 °C. The simulation results show that the ferrite PM did not experience irreversible demagnetization, i.e., above B_{thr} and below H_{thr}, under 2.6× rated current at both temperatures. When the current increased to 2.8× rated current at −40 °C and 3.4× rated current at 80 °C, the corner close to the airgap showed lower *B* than B_{thr} and higher *H* than H_{thr}. This implies that NMF-12G ferrite PM can safely operate under a 2.8× rated current at −40 °C and 3.4× rated current at 80 °C.

Table 8. Magnetic properties of NMF-12G at −40 and 80 °C.

Magnetic Property	−40 °C	80 °C
Remanent flux density (B_r) [T]	0.51	0.38
Coercivity (H_c) [kA/m]	345	299
Intrinsic Coercivity (H_{ci}) [kA/m]	350	414
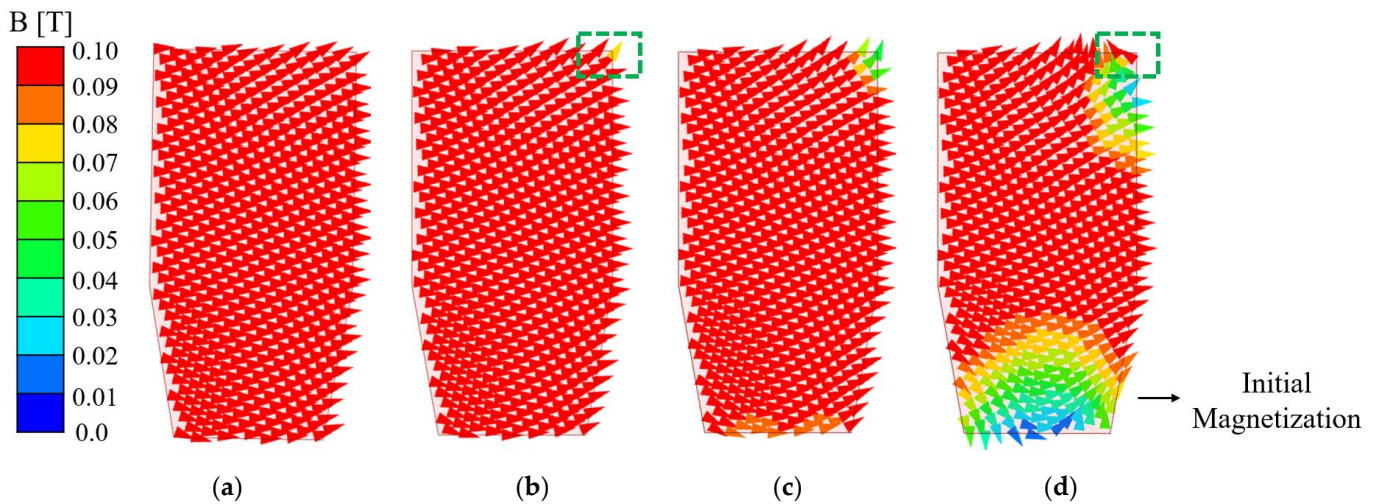
Figure 17. Flux density (*B*) distribution of 6Φ-SS-FSCW-Fer-SIPMSM at −40 °C when the motor current was (**a**) 2.6× and (**b**) 2.8× rated current, and 80 °C when the motor current was (**c**) 2.6× and (**d**) 3.4× rated current.
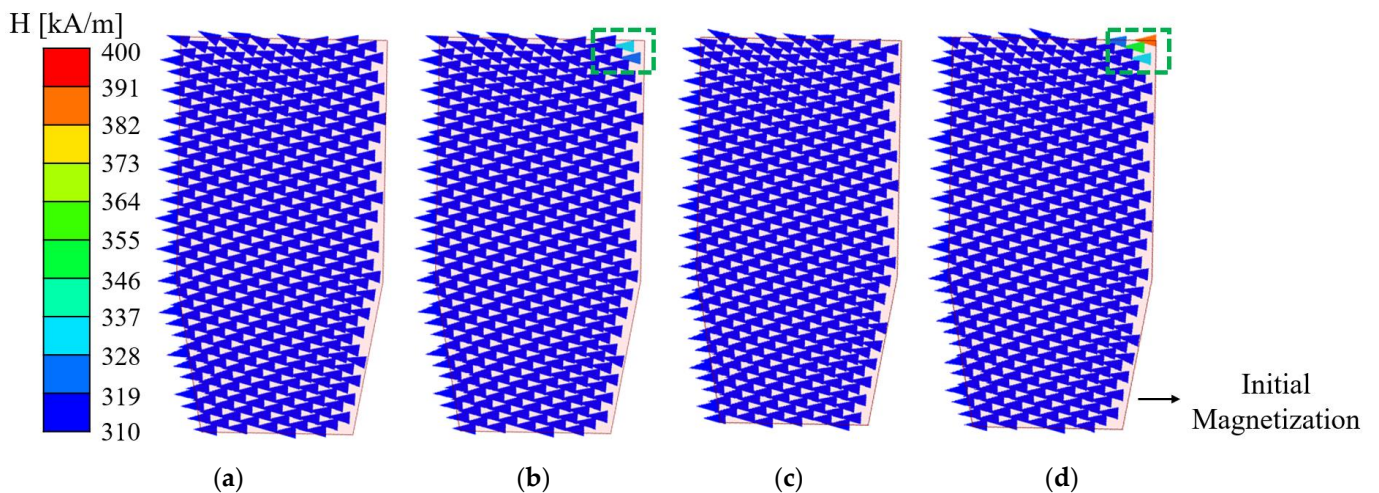

Figure 18. Magnetic field (*H*) distribution of 6Φ-SS-FSCW-Fer-SIPMSM at −40 °C when the motor current was (**a**) 2.6× and (**b**) 2.8× rated current, and 80 °C when the motor current was (**c**) 2.6× and (**d**) 3.4× rated current.

3.6. Fault-Tolerant Capability

One of the advantages of the six-phase winding configuration over the three-phase winding is the fault-tolerant capability [5]. To validate the fault-tolerant capability of the proposed six-phase machine, the motor was simulated when one of the six-phase windings was opened, i.e., I = 0. At the same time, other windings kept the same condition as a healthy case. Figure 19 shows the maximum torque profiles of the proposed machine for healthy and open-phase cases. Compared to the maximum torque for the healthy case, the average maximum torque for the open-phase case was reduced from 2.97 to 2.48 kNm, while the T_{rip} was increased from 0.9 to 50%. On the other hand, the average maximum torque and T_{rip} for the one-phase short-circuit case were increased from 2.97 to 3.2 kNm and from 0.9 to 32.5%, respectively. Although the one-phase open-circuit and short-circuit cause significant degradation in the maximum torque and T_{rip}, it is validated that the proposed motor can still operate even if one of the phases is opened and closed.
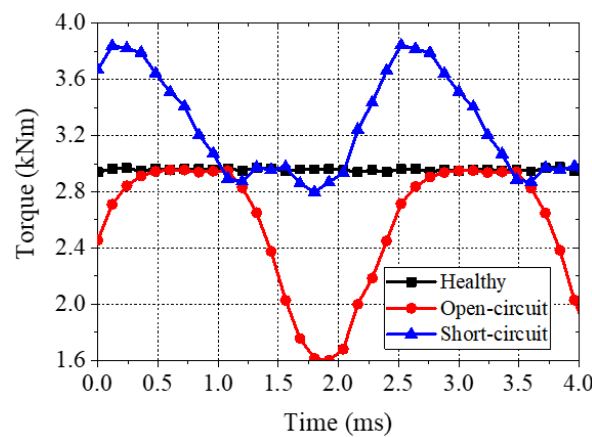

Figure 19. Torque performance of the proposed machine under healthy, 1-phase open-circuit, and 1-phase short-circuit.

4. Electric Truck Simulation Model

The dynamic model of an HDT was built and simulated using MATLAB/Simulink to assess the proposed motor performance under realistic HDT conditions. Figure 20 shows the block diagram for the HDT model, and Table 9 summarizes the vehicle specifications used in the simulation. A detailed description of each block in Figure 19 is presented below.
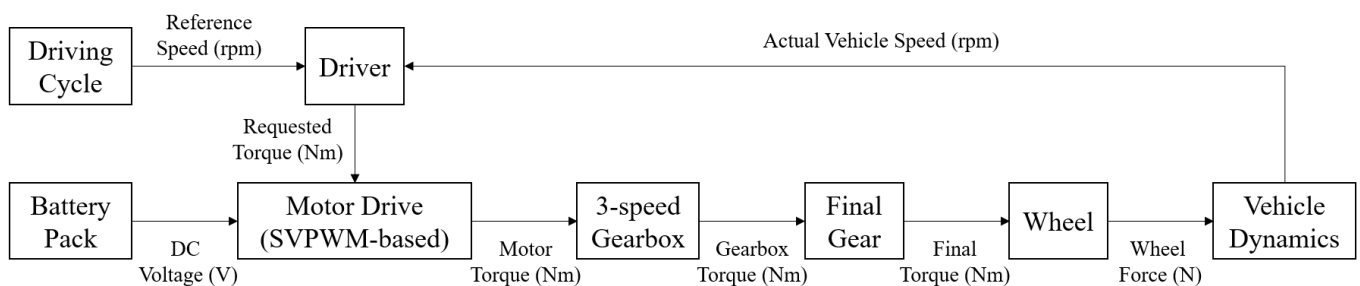
Figure 20. Overall block diagram for the dynamic model used in HDT simulation.

Table 9. Specification of the Class-7 Electric Truck Model. Data from [3].

Parameter	Symbol	Value
Vehicle mass [kg]	m_{veh}	15,227
Dynamic wheel radius [m]	R_{wheel}	0.488
Rolling resistance coefficient	C_{rr}	0.008
Coefficient of aerodynamic drag	C_d	0.6
Vehicle frontal area [m^2]	A_v	9.0

Table 9. *Cont.*

Parameter	Symbol	Value
Initial State-of-Charge [%]	SOC_{init}	100
Number of battery cell in parallel/series	$N_{parallel}/N_{series}$	53/225
Final drive gear ratio	G_{FDR}	7.17

4.1. Driver

The main objective of this block is to convert the reference driving cycle to the required motor traction and braking torque to track the reference driving cycle. The required torque (T_{req}) was calculated by applying the reference and actual vehicle speed error to a proportional-integral (PI) controller. Then, the output of the PI controller, called the applied pedal position (APP), was converted to the T_{req} by multiplying the output with the maximum motor torque of 2980 Nm.

4.2. Battery Pack

The main goal of the battery pack block is to calculate (1) the current state-of-charge ($SOC_{current}$), and (2) V_{bat} from the motor current (I_{mot}) and calculated $SOC_{current}$. First, $SOC_{current}$ is calculated by Equation (9).

$$SOC_{current} = SOC_{init} - 100 \cdot \int \frac{I_{mot}}{3600 \cdot N_{parallel}} dt, \tag{9}$$

where SOC_{init} is the initial SOC of the battery pack, and $N_{cell\_parallel}$ is the number of battery cells in parallel. These values are listed in Table 9. Based on $SOC_{current}$, V_{bat} is computed by Equation (10).

$$V_{bat} = N_{series} \left(V_{oc}(SOC_{current}) - \frac{R(SOC_{current}) \cdot I_{mot}}{N_{parallel}} \right) \tag{10}$$

where V_{oc} and R are the open-circuit cell voltage and resistance as a function of $SOC_{current}$, respectively, and N_{series} is the number of battery cells in series. Figure 21 shows V_{oc} and R as a function of $SOC_{current}$. Since both V_{oc} and R change significantly at 10% of $SOC_{current}$, the simulation stops when $SOC_{current}$ reaches 15%.
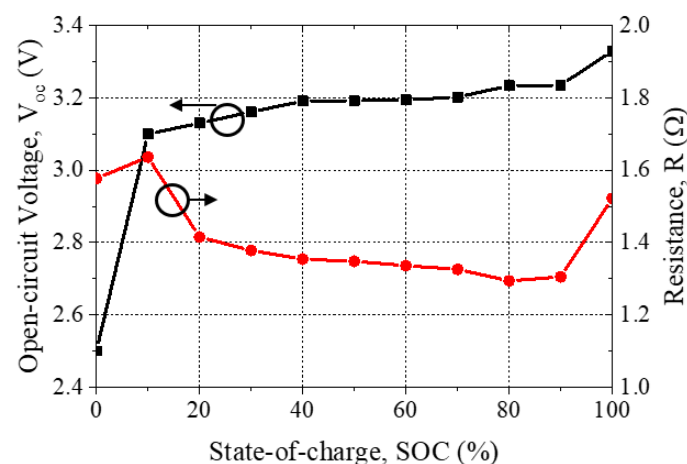

Figure 21. Open-circuit voltage and resistance versus state-of-charge.

4.3. Motor Drive

The motor drive block was used to calculate (1) T_m from T_{req} from the driver block, and (2) I_{mot} to produce T_m. A lookup table determined T_m with the maximum allowable torque at a given speed (T_{thr}), indicated by the solid black line shown in the motor efficiency map

in Figure 14. If T_{req} is below T_{thr}, then T_m equals T_{req}. On the other hand, if T_{req} is higher than T_{thr}, then T_m equals T_{thr}.

I_{mot} is calculated by Equation (11).

$$I_m = \frac{T_m \omega_m}{\left(V_{dc}/\sqrt{3}\right) \cdot \eta_m} \tag{11}$$

where η_m is each motor efficiency, as shown in Figure 14.

4.4. 3-Speed Gearbox and Final Gear

This block converted the T_m and wheel speed (ω_{wheel}) from the wheel block to the gear torque (T_{gear}) and ω_m, respectively. T_{gear} and ω_m were determined by Equations (12) and (13), respectively.

$$T_{gear} = T_m \cdot G_{1,2,3} \cdot G_{FDR}, \tag{12}$$

$$\omega_m = \omega_{wheel} \cdot G_{1,2,3} \cdot G_{FDR}, \tag{13}$$

where $G_{1,2,3}$ are the optimal three-speed gear ratios obtained in [3] under four drive cycles, and G_{FDR} is the final drive ratio of 7.66. These gear ratios of the three-speed gearbox are listed in Table 10. Figure 22 describes the flowchart for the three-speed gear shifting strategy. The details of the drive cycles are presented in the following section.

Table 10. The 3-speed optimal gear ratio under the drive cycle.

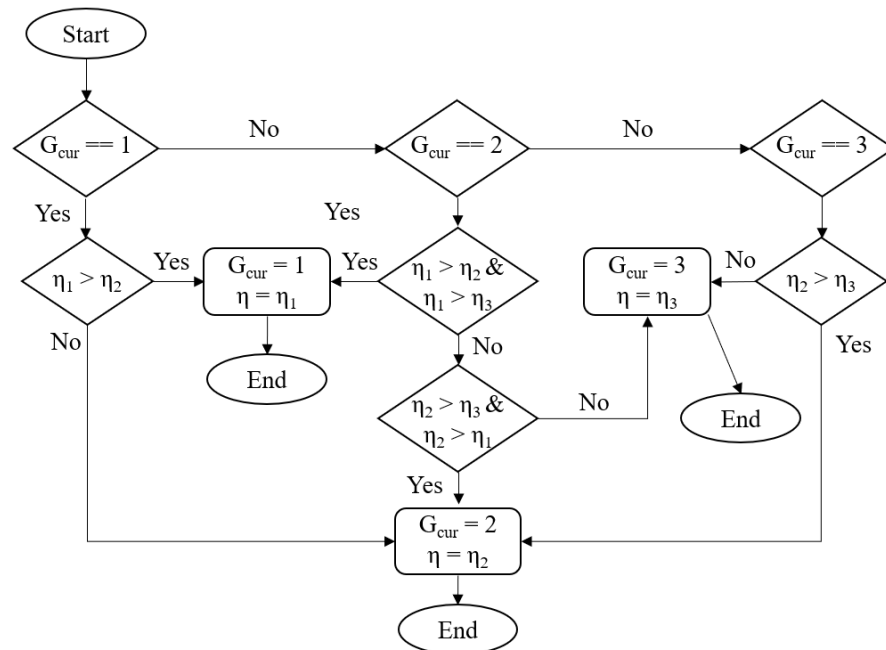| Drive Cycle	1st	2nd	3rd
CILCC	1.01	0.539	0.241
OCC	1.16	0.584	0.302
UDDSHDV	1.09	0.489	0.302
HWFET	1.01	0.416	0.259

Figure 22. Flowchart for the 3-speed gear shifting strategy.

4.5. Wheel

The wheel block was used to convert (1) the T_{gear} from the three-speed gearbox and final gear block to the traction force (F_{trac}), and (2) the vehicle speed (V_{veh}) from the vehicle dynamic block to the ω_{wheel}. F_{trac} and ω_{wheel} were calculated by Equations (14) and (15).

$$F_{trac} = T_{wheel} / R_{wheel}, \tag{14}$$

$$\omega_{wheel} = V_{veh} / R_{wheel}, \tag{15}$$

where R_{wheel} is the wheel radius, listed in Table 9.

4.6. Vehicle Dynamics

Lastly, this subsystem converted F_{trac} from the wheel block to the V_{veh}. The V_{veh} was calculated using the following equations.

$$V_{veh} = \frac{1}{M_i} \int (F_{trac} - F_{loss}) dt, \tag{16}$$

$$F_{loss} = \frac{1}{2} \rho A_v C_d (V_{veh})^2 + m_{veh} g C_{rr}, \tag{17}$$

where g is the gravity (9.8 m/s^2), and ρ is the air density (1.204 kg/m^3). Additional parameters are listed in Table 9.

5. Performance Evaluation of Proposed Motor in Electric Truck Simulation

5.1. Traction Performance

Generally, the class-7 HDTs are driven in two modes: city and inter-city. The city mode is driven like a utility service truck, requiring frequent start-stop operations, while the inter-city mode requires high-speed driving and few start-stop operations [3]. For the city mode, the Advanced Heavy Hybrid Propulsion Systems (AHHPS) program uses the combined international local and commuter cycle (CILCC) to evaluate HDTs [25]. The AHHPS is sponsored by the U.S. Department of Energy. To further evaluate in the city mode, the Urban Dynamometer Driving Schedule for Heavy Duty Vehicle (UDDSHDV) and Orange County Bus Cycle (OCC) were used. For the inner-city transportation, the Highway Fuel Economy Test (HWFET) was utilized. Figure 23 shows the driving cycles with the tracking performances of the reported and proposed PMSM. Both the reported and proposed PMSMs closely followed the reference driving cycles.
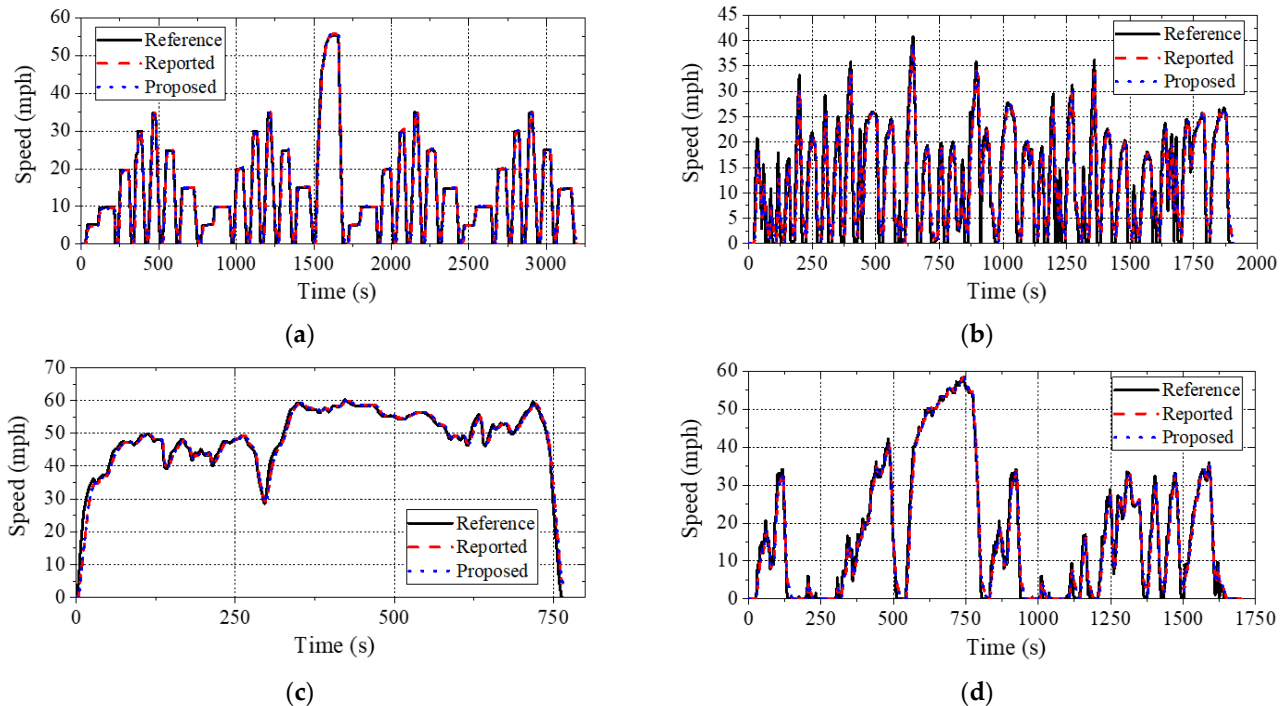

Figure 23. Tracking performance of the reported and proposed motor under (**a**) CILCC, (**b**) OCC, (**c**) HWFET, and (**d**) UDDSHDV.

5.2. Energy Consumption

Table 11 shows the energy consumption in Watt-hour (Wh) and Wh per km for the reported and proposed motor with the three-speed gearboxes. The proposed motor can save the energy by 55, 74, 28, and 90 Wh and 2.9, 5.9, 2.6, and 5.5 Wh per km in the CILCC, UDDSHDV, OCC, and HWFET driving cycle, respectively, compared to the reported motor. This implies that the proposed motor can save 1.8, 4.3, 1.9, and 3.7 kWh of energy when a 300 kWh battery is used. According to Bloomberg New Energy Finance, the average price of the battery per kWh in 2020 was USD 137 per kWh [26]. Based on this price and the calculated energy savings, the proposed motor can save USD 243.7, 589.3, 262.9, and 504 in the CILCC, UDDSHDV, OCC, and HWFET driving cycles, respectively.

Table 11. Energy consumption of the reported and proposed motor with a 3-speed gearbox under 4 drive cycles.

Drive Cycle	Energy Consumption in Wh		Energy Consumption in Wh/km		Consumption Savings [%]
	Reported 6Φ-FSCW-Nd-FIPMSM	Proposed 6Φ-SS-FSCW-Fer-SIPMSM	Reported 6Φ-FSCW-Nd-FIPMSM	Proposed 6Φ-SS-FSCW-Fer-SIPMSM	
CILCC	8485.7	8430.7	441.1	438.3	0.64
OCC	4719.6	4692.0	452.1	449.4	0.60
UDDSHDV	5658.0	5583.6	451.6	445.6	1.33
HWFET	452.0	446.5	452.0	446.5	1.22

5.3. Cost

A significant advantage of the ferrite motor over the RE-PM motor is the cost. Thereby, the costs of the reported RE-PM and proposed ferrite motor were compared to show the effectiveness of the proposed motor quantitatively. The motor cost was calculated by Equation (18):

$$\text{Machine Cost} = \left(A_{mag}\rho_{mag}C_{mag} + A_{ro}\rho_{M19}C_{M19} + A_{st}\rho_{M19}C_{M19} + A_{nm}\rho_{nm}C_{nm} \right)L + M_{cu}C_{cu}, \tag{18}$$

where A denotes the area for each material, ρ is the density, and C is the material cost per kg. The subscripts correspond to mag = magnet (NdFeB for the reported motor and NMF-12G for the proposed motor), $M19$ = M19–29G (non-oriented Si-steel), Cu = copper, nm = nonmagnetic wedge for the proposed motor only, L = the stack length of the motor, and M = the mass of the material. The cost and density of each material are listed in Table 12 [13,14]. The costs of the shaft, lamination between stacked cores, and housing with liquid cooling are excluded. Based on the prices listed in Table 12, the volume, weight, and cost of the reported and proposed motor are calculated and summarized in Table 13. These results show that the proposed motor can be fabricated not only 42 kg lighter but also with a USD 2512 lower cost than the reported motor. This cost reduction is mainly attributed to the significantly lower price of the ferrite PM than the RE-PM.

Table 12. Material cost and density.

Material	Cost ($/kg)	Density (g/cm^3)
NdFeB	100	7.5
Ferrite	7	5
Copper	7.03	8.96
CuBe alloy	165	1
M19–29G	1.0	7.85

Table 13. Volume, weight, and cost of the reported and proposed motor.

Part	Reported			Proposed			Cost Savings [%]
	Volume [cm^3]	Weight [kg]	Cost [\$]	Volume [cm^3]	Weight [kg]	Cost [\$]	
Stator	31,105	244.1	244	31,261	245.4	245	0
Rotor	19,819	155.6	156	14,234	111.8	112	28
Magnet	3570	26.8	2677	5467	27.4	191	92.9
Coil	15,066	135	949	15,066	135	949	0
Wedges	0	0	0	100.5	0.15	16.6	−16,600
Total		561	4026		519	1514	62.4

6. Conclusions

This paper proposed a 6-phase (dual 3-phase) 24-slot/10-pole stator-shifted fractional-slot concentrated winding spoke-type ferrite permanent magnet motor for class-7 electric truck application. By adopting a stator-shifting concept and an 11 mm diameter circular notch embedded in the rotor, the proposed motor generated a maximum torque of 2980 Nm and a torque ripple of 0.9%. This low torque ripple is attributed to the significantly reduced MMF harmonic order of the 7th, 17th, 19th, and 29th, resulting in 86% torque ripple reduction with 28% torque improvement. The simulated results of the stator-shifted motor were in good agreement with the measured results of the stator-shifted prototype. The irreversible demagnetization and mechanical analysis showed that the proposed motor could operate up to the operating current of 3.8× of the rated current under extreme temperature and at its maximum speed of 3750 rpm without any issue. An electric truck model was constructed and simulated using MATLAB/Simulink to evaluate the proposed motor performance. The simulation results showed that compared to the reported NdFeB-based motor, the proposed ferrite motor could save not only the battery capacity of 2.6–5.9 Wh/km, which is equivalent to USD 244–589 when a 300 kWh battery is used, but also the motor cost of USD 2512 while showing similar motor performance.

7. Patents

The U.S. provisional patent entitled "Ferrite Spoke-type Permanent Magnet Synchronous Motor for Electric Truck" is under review by the U.S. patent office.

Author Contributions: Conceptualization, H.W. and Y.-K.H.; methodology, H.W.; software, H.W. and J.P.; validation, H.W. and J.P.; formal analysis, H.W.; investigation, H.W.; resources, Y.-K.H.; data curation, H.W.; writing—original draft preparation, H.W.; writing—review and editing, Y.-K.H., M.C., B.B., S.C., S.L., H.-S.Y. and T.A.H.; visualization, H.W.; supervision, Y.-K.H.; project administration, J.L., T.L. and T.-W.L.; funding acquisition, Y.-K.H. and T.-W.L. All authors have read and agreed to the published version of the manuscript.

Institutional Review Board Statement: Not applicable.

Informed Consent Statement: Not applicable.

Data Availability Statement: Data sharing not applicable.

References

1. Smith, D.; Graves, R.; Ozpineci, B.; Jones, T.; Lustbader, J.; Kelly, K.; Walkowicz, K.; Birky, A.; Payne, G.; Sigler, C.; et al. *Medium- and Heavy-Duty Vehicle Electrification An Assessment of Technology and Knowledge Gaps; ORNL/SPR-2020/7*; Oak Ridge National Lab.(ORNL): Oak Ridge, TN, USA, 2019; pp. 1–60.
2. U.S. PIRG Education Fund, Environment America Research and Policy Center, Frontier Group. Available online: https://environmentamerica.org/feature/ame/electric-buses-america (accessed on 22 August 2021).

3.   Morozov, A.; Humphries, K.; Zou, T.; Rahman, T.; Angeles, J. Design, analysis and optimization of a multi-speed powertrain for class-7 electric truck. *SAE Int. J. Alt. Power.* **2018**, *7*, 27–42. [CrossRef]
4.   Patel, V.; Wang, J.; Wang, W.; Chen, X. Six-phase fractional-slot-per-pole-per-phase permanent-magnet machines with low space harmonics for electric vehicle application. *IEEE Trans. Ind. Appl.* **2014**, *50*, 2554–2563. [CrossRef]
5.   Abdel-Khalik, A.; Ahmed, S.; Massoud, A. A six-phase 24-Slot/10-pole permanent magnet machine with low space harmonics for electric vehicle applications. *IEEE Trans. Magn.* **2016**, *52*, 8700110. [CrossRef]
6.   Cheng, L.; Sui, Y.; Zheng, P.; Yin, Z.; Wang, C. Influence of stator MMF harmonics on the utilization of reluctance torque in six-phase PMA-SynRM with FSCW. *Energies* **2018**, *11*, 108. [CrossRef]
7.   Bianchi, N.; Bolognani, S.; Pre, M.; Grezzani, G. Design considerations for fractional-slot winding configuration of synchronous machines. *IEEE Trans. Ind. Appl.* **2006**, *42*, 907–1006. [CrossRef]
8.   Tangudu, J.; Jahns, T.; El-Refaie, A. Unsaturated and saturated saliency trends in fractional-slot concentrated-winding interior permanent magnet machines. In Proceedings of the IEEE Energy Conversion Congress and Exposition (ECCE), Atlanta, GA, USA, 12–16 September 2010.
9.   Alberti, L.; Bianchi, N. Theory and Design of Fractional-slot Multilayer Windings. *IEEE Trans. Ind. Appl.* **2013**, *49*, 841–849. [CrossRef]
10. Dajaku, G.; Gerling, D. Eddy current loss minimization in rotor magnets of PM machines using high-efficiency 12-teeth/10-slots winding topology. In Proceedings of the 2011 International Conference on Electrical Machines and Systems, Beijing, China, 20–23 August 2011.
11. Dajaku, G. Elektrische Maschine. German Patent DE 102008 057349 B3, 15 July 2010.
12. Jeong, C.; Hur, J. A novel proposal to improve reliability of spoke-type BLDC motor using ferrite permanent magnet. *IEEE Trans. Ind. Appl.* **2016**, *52*, 3814–3821. [CrossRef]
13. Won, H.; Hong, Y.; Choi, M.; Bryant, B.; Platt, J.; Choi, S. Cost-effectiveness hybrid permanent magnet assisted synchronous reluctance machine for electric vehicle. In Proceedings of the IEEE International Electric Machines and Drives Conference, Online, 17–20 May 2021.
14. Ma, Q.; ElRefaie, A.; Lequesne, B. Low-cost interior permanent magnet machine with multiple magnet types. *IEEE Trans. Ind. Appl.* **2020**, *56*, 1452–1463. [CrossRef]
15. Kimiabeigi, M.; Widmer, J.; Long, R.; Gao, Y.; Goss, J.; Martin, R.; Lisle, T.; Soler Vizan, J.; Michaelides, A.; Mecrow, B. On selection of rotor support material for a ferrite magnet spoke-type traction motor. *IEEE Trans. Ind. Appl.* **2016**, *52*, 2224–2233. [CrossRef]
16. Zhao, W.; Lipo, T.; Kwon, B. Torque pulsation minimizations in spoke-type interior permanent magnet motors with skewing and sinusoidal permanent magnet configurations. *IEEE Trans. Magn.* **2015**, *51*, 1–6.
17. Won, H.; Hong, Y.; Platt, J.; Choi, M.; Bryant, B.; Choi, S. Six-phase fractional-slot concentrated winding ferrite spoke-type permanent magnet synchronous motor for electric truck. In Proceedings of the IEEE International Electric Machines and Drives Conference, Online, 17–20 May 2021.
18. N42UH Arnold Magnetic Technologies. Available online: http://www.arnoldmagnetics.com/wp-content/uploads/2017/11/N42UH-151021.pdf (accessed on 23 February 2022).
19. El-Refaie, A.; Alexander, J.; Galioto, S.; Reddy, P.; Huh, K.; Bock, P.; Shen, X. Advanced high-power density interior permanent magnet motor for traction applications. *IEEE Trans. Ind. Appl.* **2014**, *50*, 3235–3248. [CrossRef]
20. Abdel-Khalik, A.; Ahmed, S.; Massoud, A. Low space harmonics cancellation in double layer fractional slot winding using dual multi-phase winding. *IEEE Trans. Magn.* **2015**, *51*, 8104710. [CrossRef]
21. Rashid, M. *Power Electronics: Circuits, Devices and Applications*, 3rd ed.; Prentice Hall: London, UK, 2004; pp. 919–923.
22. Li, Y.; Li, C.; Garg, A.; Gao, L.; Li, W. Heat dissipation analysis and multi-objective optimization of a permanent magnet synchronous motor using surrogate assisted method. *Case Stud. Therm. Eng.* **2021**, *27*, 101203. [CrossRef]
23. Ferrite Summary, TDK. Available online: https://product.tdk.com/en/system/files?file=dam/doc/product/ferrite/ferrite-core/catalog/ferrite_summary_en.pdc (accessed on 23 February 2022).
24. Permanent Magnets, Hitachi. Available online: https://www.hitachimetals.com/materials-products/permanent-magnets/documents/Permanent_Magnets.pdf (accessed on 23 February 2022).
25. Zou, Z.; Davis, S.; Beaty, K.; O'Keefe, M.; Hendricks, T.; Rehn, R.; Weissner, S.; Sharma, V. A new composite drive cycle for heavy-duty hybrid electric class 4–6 vehicles. *SAE Trans. J. Eng.* **2004**, *113*, 771–778.
26. Green Car Reports. Available online: https://www.greencarreports.com/news/1132072_report-60-kwh-battery-pack-price-will-make-evs-cheaper-than-combustion (accessed on 22 August 2021).